



Cite this: *RSC Adv.*, 2023, 13, 22325

# Impact of surface cooling on the water harvesting efficiency of nanostructured window glass†

Yoonseo Do,<sup>a</sup> Minji Ko<sup>bc</sup> and Young Kwang Lee \*<sup>c</sup>

Humans face a severe shortage of fresh water due to economic growth, climate change, overpopulation, and overutilization. Atmospheric water harvesting (AWH) is a promising solution where clean water is collected from the air through various approaches, including dropwise condensation. However, designing surfaces that balance rapid condensation with efficient water removal is challenging. To address this issue, inspired by the efficient water collection mechanisms in the skin of cold-blooded tree frogs, we propose an eco-friendly approach to collect fresh water from cooled window glass. We fabricated various planar and TiO<sub>2</sub> nanostructured surfaces including surfaces mimicking a lotus leaf and a hybrid surface mimicking a desert beetle and a cactus, with different wettability levels such as superhydrophilic, hydrophilic, hydrophobic, superhydrophobic, and biphilic. Sub-cooling of glass substrates between 5 and 15 °C using a Peltier device significantly enhanced the condensation process for all surfaces, with modest dependency on surface properties. This cooling temperature regime could be achieved by geothermal cooling methods that consume little energy. To improve visibility for window applications, we developed hydrophobic polymer nanofilm-modified glass substrates using a simple spin-coating technique, and achieved comparable water harvesting efficiency to that of nanostructured substrates. Our study provides insight into the optimal surface structures and cooling temperature for window glass AWH systems that could be used with an underground cooling system.

Received 23rd May 2023

Accepted 18th July 2023

DOI: 10.1039/d3ra03433j

rsc.li/rsc-advances

## 1. Introduction

The global shortage of fresh water is rapidly worsening due to continued economic development, climate change, and indiscriminate use, resulting in a significant rise in the population facing water scarcity.<sup>1,2</sup> It has been estimated that in about 30 years, 4 billion people will suffer from water scarcity.<sup>1–4</sup> To address this issue, researchers have developed various approaches, with atmospheric water harvesting (AWH) being one of the best solutions for collecting clean water from the air.<sup>5–8</sup> Research teams have developed various AWH techniques, including fog or dew harvesting, dropwise condensation, and absorption-based water harvesting.<sup>9–12</sup> The dropwise condensation process is a promising approach for effectively collecting fresh water from the air, even in arid and semi-arid areas.<sup>13,14</sup> This process can be assisted by a cold surface below the dew point, but it is challenging to provide sufficient condensation sites while simultaneously removing the water droplets.<sup>15</sup>

The efficiency of water harvesting can be increased by lowering the cooling temperature, but this comes at the cost of

increased energy consumption. However, a few cold-blooded animals such as the *Litoria caerulea* tree frog<sup>16</sup> and the Australian *Moloch horridus* desert lizard<sup>17</sup> use their cold bodies to condense moisture from dry air through the skin using the capillary force of nanostructures.<sup>18,19</sup> Similarly, various active AWH devices, including refrigeration systems powered by solar cells, decreased the surface temperature to condense water droplets.<sup>20–24</sup> Energy-efficient passive AWH systems that combine unique surface structures and radiative cooling technologies are aimed at maximizing water harvesting without external energy consumption.<sup>25–27</sup> Radiative cooling, which only uses radiative cooling materials to cool the condensation surface, is becoming a strategic research area for AWHs.<sup>27–31</sup> Another passive AWH system is the underground cooling system, also known as Canadian wells,<sup>31–33</sup> which uses the underground temperature, around 8–12 °C at a depth of 1.2 m,<sup>34,35</sup> to cool the surface in warm, dry areas.

The efficiency of water harvesting on an engineered surface is directly proportional to its ability to mimic nature's AWH surface. The surface structures of desert beetles and cacti, which efficiently collect water in arid environments, have inspired many AWH concepts.<sup>3,36–38</sup> Most efforts to improve AWH efficiency by mimicking natural surfaces have focused on replicating the bumpy structure of beetles or the needle structure of cacti.<sup>39,40</sup> The Namibian desert beetle primarily uses a complex hybrid surface with hydrophilic bumps and

<sup>a</sup>Grier School, Pennsylvania 16686-0308, USA

<sup>b</sup>Department of Chemistry, Kookmin University, Seoul 02707, Korea

<sup>c</sup>Department of Chemistry and Biochemistry, San Diego State University, San Diego, CA 92182, USA. E-mail: [youngkwang.lee@sdsu.edu](mailto:youngkwang.lee@sdsu.edu)

† Electronic supplementary information (ESI) available. See DOI: <https://doi.org/10.1039/d3ra03433j>


a hydrophobic background to collect water in hot, dry regions. Recent research has shown that mimicking the combined structure of the desert beetle and cactus can significantly enhance water harvesting efficiency.<sup>3,41–43</sup> However, these three-dimensional structures are unsuitable for smooth and flat surfaces such as window glass.

In this study, we propose an innovative eco-friendly approach to address water scarcity by collecting water from fog on window glass surfaces. As window glass can be found in all buildings and locations, this approach provides a practical solution for collecting water in everyday life. This approach could combine the quick condensation and rapid removal functions of water droplets on cold superhydrophobic surfaces (Fig. 1a). A sustainable underground cooling system, along with a nanostructured surface of glass mimicking the superhydrophobicity of the lotus leaf, could be utilized in future applications to cool the surface below the dew point for rapid condensation.<sup>18,19,44,45</sup> Passive cooling can be achieved by injecting cool air from underground<sup>46,47</sup> into the space between double-panel windows, thereby lowering energy consumption. In addition, vertically arranged superhydrophobic window glasses also use gravity to facilitate dewetting and removal of water droplets (Fig. 1b). This system efficiently condenses water from the air but can also be turned off to allow visibility through the glass. We conducted a proof of concept study to assess the suitability of different types of glass surfaces for use in a cooled AWH system. We employed Peltier plates as cooling holders, as shown in Fig. 1c. Also, as in the majority of studies that evaluate the atmospheric water harvesting ability according to the substrate surface structures, this study utilized continuous saturated fog flow instead of harvesting water from the outdoor environment. It is worth noting that windows have traditionally been used as protection while allowing natural light into rooms, providing a view of the surroundings. This study thus also analyzes changes in the transparency and visibility of the glass according to its degree of hydrophobicity or hydrophilicity before wetting. This information will provide essential data for optimizing the window glass surface and cooling temperature in passive window-based AWH systems.

Previous studies have shown that the water harvesting capability varies with sub-cooling temperatures, which refers to the temperature difference between the surface temperature where water condenses and the ambient temperature on different substrate materials.<sup>48–51</sup> Limited studies have focused on water harvesting from glass surfaces in ambient temperature environments.<sup>52–57</sup> In-depth studies meanwhile have yet to be conducted on water harvesting from dew or fog on engineered window-glass surfaces as a function of cooling temperatures. Here, we analyzed the effect of cooling temperatures on the water collection rate of various 2D-TiO<sub>2</sub> nanostructures and plain TiO<sub>2</sub>-coated glass substrates with different wettability surfaces before and after coating a (heptadecafluoro-1,1,2,3-tetra-hydrodecyl)trichlorosilane (HDFS) self-assembled monolayer (SAM), including superhydrophilic, hydrophilic, hydrophobic, superhydrophobic, and biphilic surfaces, as shown in Fig. 2. We also investigated the water collection rate of superhydrophobic polytetrafluoroethylene (PTFE) polymer nanofilm-

coated glass substrates to maintain visibility through the modified glass. Our results provide insight into suitable surface structure for a window glass AWH system that is cooled by an underground cooling system.

## 2. Materials and methods

### 2.1. Materials

1  $\mu\text{m}$  size of polystyrene (PS) microbeads solution (Playscale, Inc.), (heptadecafluoro-1,1,2,3-tetra-hydrodecyl)trichlorosilane (HDFS) (JSI Silicone, Inc.), sodium dodecyl sulfate solution (SDS, Sigma-Aldrich), and polytetrafluoroethylene preparation (PTFE) (60 wt% dispersion in H<sub>2</sub>O, Sigma-Aldrich) was prepared. The 1  $\mu\text{m}$  size of PS microbead solution was purchased from Polysciences, Inc. to realize TiO<sub>2</sub> nanopillars as a dry etching mask. HDFS was purchased for surface treatment from JSI Silicone Inc. In addition, PTFE (60 wt% dispersion in H<sub>2</sub>O) and SDS were purchased from Sigma-Aldrich.

### 2.2. Fabrication of micro-patterned TiO<sub>2</sub> nanopillar structure and hydrophobic polymer nanofilm-coated glass substrate

To fabricate TiO<sub>2</sub> nanopillars with a diameter of 500 nm, a 200 nm Al mask layer, and a 1  $\mu\text{m}$  TiO<sub>2</sub> layer were deposited on a 5  $\times$  5 cm<sup>2</sup> glass *via* an e-beam evaporator as shown in Fig. 1. In the first mask layer, a 1  $\mu\text{m}$  PS microbeads monolayer was transferred to the Al/TiO<sub>2</sub>/glass substrate using nanosphere lithography.<sup>58</sup> As described above, the Si substrate to float the 1  $\mu\text{m}$  of PS microbeads on the water was subjected to UV-O<sub>3</sub> for two hours to form a sufficiently hydrophilic surface. The prepared 1  $\mu\text{m}$  of PS microbead solution was dropped slowly on the UV-O<sub>3</sub> treated Si substrate, and the dropped PS microbead solution was floated on water. The application of a few drops of SDS solution modified the surface tension of the water, forming a rigid and dense close-packed monolayer of 1  $\mu\text{m}$  PS. Subsequently, the 1  $\mu\text{m}$  PS microbeads were transferred onto the deposited Al/TiO<sub>2</sub>/glass substrate. To fabricate TiO<sub>2</sub> nanopillar with a diameter of 500 nm, the well-ordered 1  $\mu\text{m}$  PS microbeads monolayer was decreased to 500 nm using O<sub>2</sub> plasma with a reactive ion etcher (RIE; PlasmaPro 80 RIE, Oxford Instruments). The Al layer for the hard mask of the TiO<sub>2</sub> layer was etched by Cl<sub>2</sub>-based inductively coupled plasma (ICP; PlasmaPro 100 Cobra, Oxford Instruments) using the decreased 500 nm PS microbeads as the first mask layer. In order to realize TiO<sub>2</sub> nanopillar with various heights of 100 nm, 300 nm, and 500 nm, the TiO<sub>2</sub> layer was etched *via* SF<sub>6</sub>, CHF<sub>3</sub>, and Ar-based RIE using the decreased Al layer. Finally, the Al layer was removed by Al etchant. For the realization of various surface structures with wettability of the fabrication TiO<sub>2</sub> nanopillar: superhydrophobic, hydrophobic, and biphilic, the surface of the TiO<sub>2</sub> nanopillar for superhydrophobic and hydrophobic surfaces was modified using liquid phase self-assembled monolayers (SAMs) with 0.05 vol% of HDFS in hexane solution for 30 min. To realize a biphilic TiO<sub>2</sub> nanopillar surface, the treated superhydrophobic TiO<sub>2</sub> nanopillar substrate was UV-O<sub>3</sub> irradiated for one hour through a triangle micro-patterned



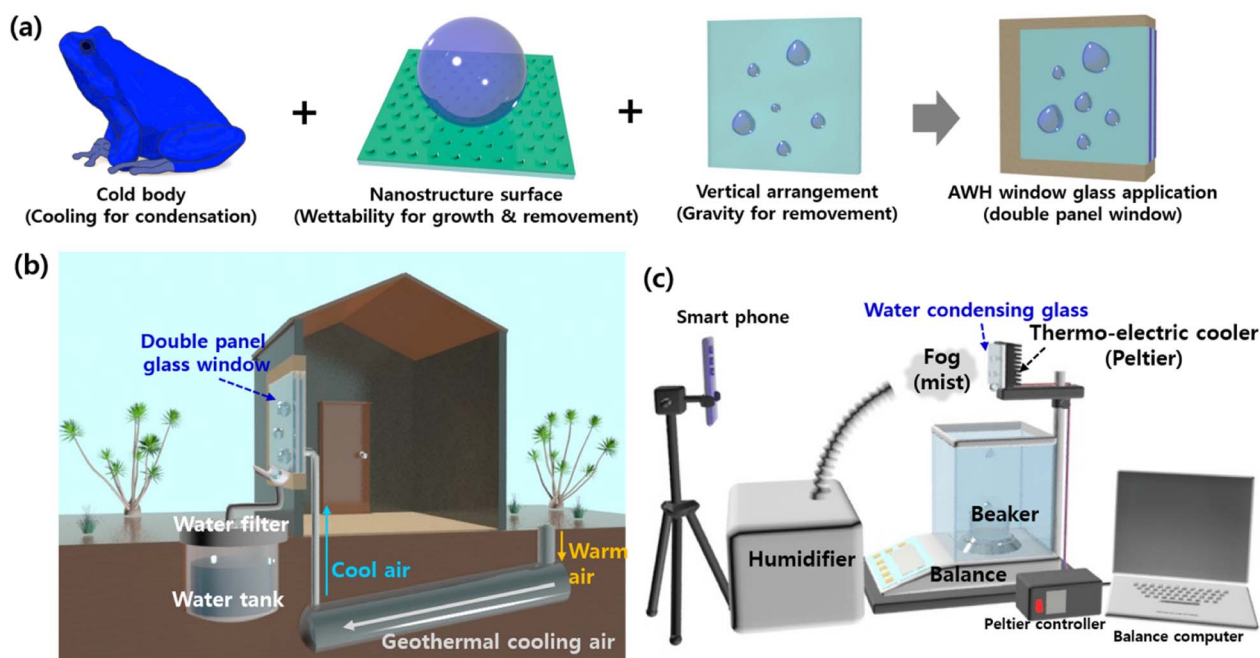


Fig. 1 (a) Schematic diagram of our strategies to develop the efficient AWH device: passive cooling, nanostructured surface, and vertical arrangement. (b) Underground cooling manner (Canadian wells) assisted double-panel glass for window AWH system. (c) Schematic diagram of Peltier-cooling water-collecting system with varying glass with wettability and temperature.

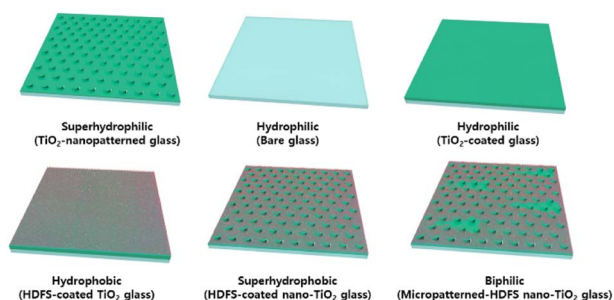


Fig. 2 Various surface structures with wettability: superhydrophilic, hydrophilic, hydrophobic, superhydrophobic, and bipilic (hydrophilic micro-pattern and hydrophobic background).

mask with different dimensions of the  $x$ -axis: 100  $\mu\text{m}$ , 200  $\mu\text{m}$ , and 300  $\mu\text{m}$ .<sup>59–61</sup>

To realize a hydrophobic polymer nanofilm-coated glass substrate, the glass substrate was first treated with UV- $\text{O}_3$  for 330 seconds. A PTFE solution was then diluted in  $\text{H}_2\text{O}$  (1 : 2 volume ratio) to obtain high transmittance. The diluted PTFE solution was coated on UV- $\text{O}_3$ -treated glass substrates with various coating speeds: 1000 rpm, 2000 rpm, and 3000 rpm for 60 seconds. The PTFE-coated glass substrates were dried at 120  $^\circ\text{C}$  for 12 hours in a vacuum oven.

### 2.3. Water collecting set-up and measurement

Fig. 1c shows a schematic diagram of the water collecting system where various glass substrates are placed on a Peltier cooling module. A commercial humidifier introduces fog mist

onto condensing substrates, sprayed in the air, and this is condensed into liquid water on the surface of cold glass substrates. The water collecting experiment was performed while the temperature and humidity in the room measured with a thermo-hygrometer were maintained at  $24.5 \pm 0.5$   $^\circ\text{C}$  and  $40 \pm 5\%$ , respectively. The condensing glass substrate measured by the attached thermocouple is maintained at temperatures of 5.0, 10.0, 15.0, and  $20.0 \pm 0.3$   $^\circ\text{C}$ , respectively, below the dew point of 21–23  $^\circ\text{C}$  by controlling the Peltier cooling module. Water droplets falling vertically are collected in a beaker under the glass substrate and measured automatically by computer-connected balance every minute for 5 h. The water collection rate was calculated using the equation  $M = M/St$ , where  $M$  is the water collection weight of mg,  $S$  is the fog-capturing substrate area of  $\text{m}^2$ , and  $t$  is the collection time (here, 5 h). A smartphone camera imaged the condensation, growth, and removal behavior every minute for 40 min.

## 3. Results and discussion

We introduced 2D nanopillar structures and HDFS-SAM coatings on  $\text{TiO}_2$  film-coated glass surfaces to fabricate glass with different levels of wettability. The wettability was controlled by varying the height of the  $\text{TiO}_2$  nanopillar between 100 and 500 nm with or without HDFS-SAM coatings. We used fabrication processes such as  $\text{TiO}_2$  film coating, mask coating, nanosphere lithography, dry-etching, and SAM coating to produce these nanopillar-engineered surfaces. As shown in Fig. 3a, 2D  $\text{TiO}_2$  nanopillar patterns on a glass substrate were fabricated using an ashing process for a PS nanosphere soft mask and a subsequent dry-etching process for an Al hard mask and  $\text{TiO}_2$





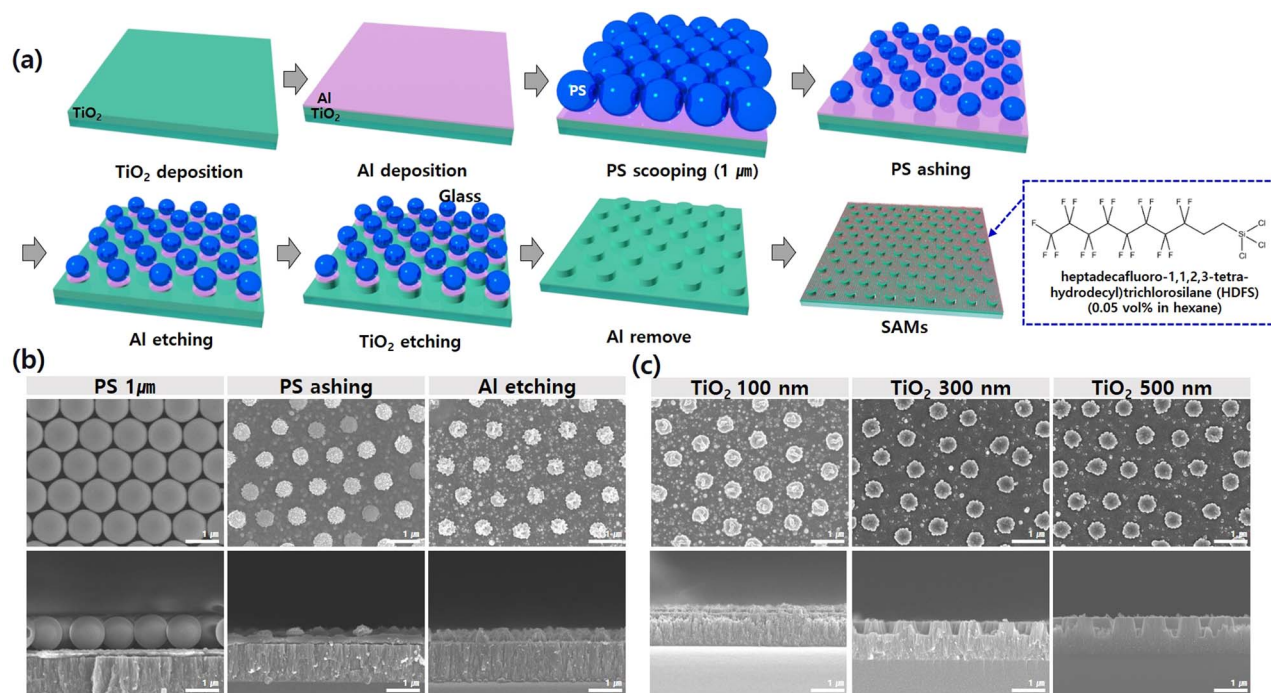


Fig. 3 (a) Schematic diagram of 2-D TiO<sub>2</sub> nanopillar fabrication process on the glass surface and HDFS-coated 2D nanopillar. (b) SEM images of the top and side views of 2-D PS mask array, ashed 2-D PS mask array, 2-D Al mask array. (c) SEM images of the top and side views of 100 nm, 300 nm, and 500 nm heights of TiO<sub>2</sub> nanopillar arrays in the fabrication process of 2-D nanopillars on the glass substrate.

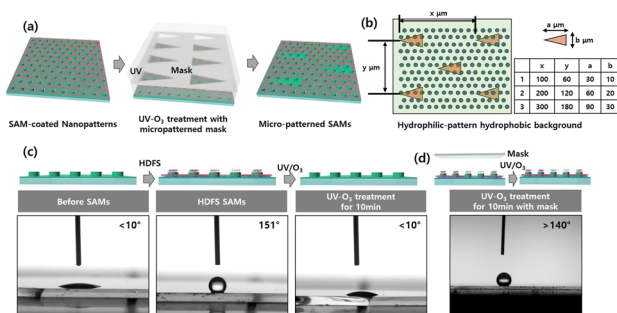


Fig. 4 (a) The fabrication of hydrophilic micropattern-hydrophobic background structure using micropatterned mask and UV-O<sub>3</sub> irradiation. (b) Dimension of hydrophilic micropattern-hydrophobic background surfaces fabricated on the glass substrate; table indicated three different dimensions of triangle patterns. (c) Optical pictures showing the conversion from superhydrophilic to superhydrophobic surfaces by HDFS coating, and from superhydrophilic to superhydrophilic surfaces due to the decomposition of HDFS by UV-O<sub>3</sub> treatment. (d) Mask-covered UV-O<sub>3</sub> treatment of superhydrophobic glass substrate.

nanopillars. Fig. 3b shows side and top SEM images of the intermediate steps to produce 2D TiO<sub>2</sub> nanopillars. Fig. 3c shows the cross-sectional and plane view of SEM images of 2D TiO<sub>2</sub> nanopillars with different heights. The SEM images confirmed that the combined nanosphere lithography and top-down etching process produced uniformly distributed 2D TiO<sub>2</sub> nanopillar arrays on a 5 × 5 cm<sup>2</sup> glass substrate with 100, 300, and 500 nm heights. Next, a plain TiO<sub>2</sub> film-coated glass and 2D TiO<sub>2</sub> nanopillar patterned glasses were immersed in HDFS

solution to change the wettability from hydrophilic to hydrophobic.

Fig. S1† shows the change in contact angle of the plain TiO<sub>2</sub> film-coated glass and various 2D TiO<sub>2</sub> nanopillar patterned glasses before and after HDFS coatings. Before applying the HDFS coating, the wettability of TiO<sub>2</sub> nanopillar patterned glass increased as the height of the pillars increased. However, after applying the HDFS coating, the hydrophobicity of the surfaces was varied. The surface that was initially the most hydrophilic became the most hydrophobic. 2D TiO<sub>2</sub> nanopillars, which have a height of 500 nm and a diameter of approximately 500 nm, exhibited a superhydrophilic surface in the absence of the HDFS coating and a superhydrophobic surface in the presence of HDFS coating. Contact angle measurements confirmed that the surface wettability could be controlled from superhydrophilicity (<10°) to superhydrophobicity (>150°) (Fig. S1†). Engineered glass was then secured to study the effect of cooling temperatures on the AWH efficiency of glass substrates with various wettability.

In addition, we created a biphilic surface that displays micropatterned HDFS layer on a 2D TiO<sub>2</sub> nanopillar-patterned glass substrate. For this, a HDFS layer was locally removed by UV-O<sub>3</sub> treatment applied through a micro-patterned photo-mask. This creates a hydrophilic micropattern on a hydrophobic background, mimicking the desert beetle's back, as shown in Fig. 4a. We chose cactus-cone-shaped micropattern arrays (isosceles triangle arrays), as seen in Fig. 4b. Previous studies have reported that the triangle shape provides excellent AWH capability to collect water from air among different

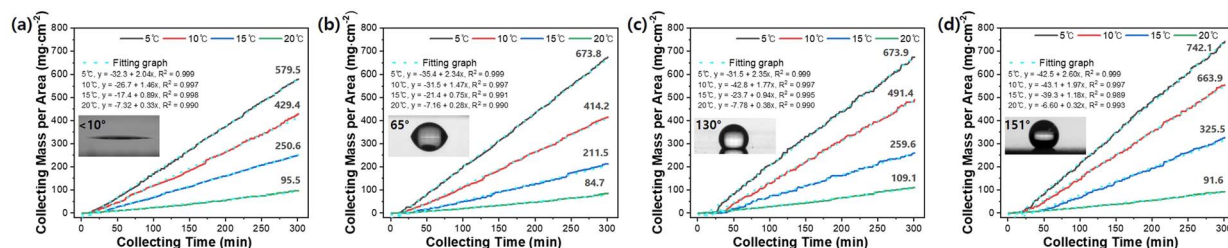


Fig. 5 Water collecting mass per unit area of four representative glasses with wettability as a function of collecting time for 5 h and the cooling temperature: (a)  $\text{TiO}_2$  nanopillar arrays with 500 nm of height; superhydrophilic, (b)  $\text{TiO}_2$  plain film; hydrophilic, (c) HDFs-coated  $\text{TiO}_2$  plain film; hydrophobic, (d) HDFs-coated  $\text{TiO}_2$  nanopillar arrays with 500 nm of height; superhydrophobic.

micropattern shapes.<sup>39</sup> Fig. 4c demonstrates that the complete coating of HDFs on 500 nm 2D  $\text{TiO}_2$  nanopillar glass changes its surface wettability from superhydrophilic ( $<10^\circ$ ) to superhydrophobic ( $>150^\circ$ ). The  $\text{UV-O}_3$  treatment then recovers the surface from superhydrophobic to superhydrophilic by photocatalytically decomposing HDFs SAMs by the  $\text{TiO}_2$  surface. In addition, mask-covered  $\text{UV-O}_3$  treatment preserves the glass substrate contact angle of  $140^\circ$  or more (Fig. 4d). Contact angle changes demonstrate that hydrophilic micropatterns can be generated on a hydrophobic substrate using the micropatterned mask. The contact angle of the biphilic substrate is slightly lower than that of the superhydrophobic glass substrate because the superhydrophilic micropatterned region is much smaller than the superhydrophobic background region. This biphilic micropattern was obtained by UV-screening of the superhydrophobic surface with a micro-patterned mask, which only caused a photocatalytic decomposition reaction in the desired area, creating superhydrophilic micropatterns. As indicated in the inset table, three types of biphilic substrates were created by varying the size and spacing of triangular patterns. As shown in Fig. S2,† the contact angle of the biphilic surface regularly decreases as the area of the superhydrophilic isosceles triangle increases, even if the superhydrophilic and superhydrophobic area ratios are similar. This result indirectly confirmed that we obtained a biphilic surface on the glass substrates.

Fig. S3† illustrates a Peltier-based fog-collecting system that we used to assess the water-harvesting capacity of nine glass

substrate surfaces with varying contact angles. The collected water from these nine surfaces was measured over five hours at different cooling temperatures (Fig. S4†). The glass substrate was placed vertically on the Peltier device to measure the mass of water droplets dripping from the glass with various surface structures (Fig. S3b†). The Peltier cold-side plate precisely controls the temperature of the glass substrate between  $5$  and  $20 \pm 0.5^\circ\text{C}$  at an atmospheric temperature of  $24.5 \pm 0.5^\circ\text{C}$  and humidity of  $40 \pm 5\%$ . The balance automatically measures the mass collected in a weighing beaker once every minute. This water-collecting setup provides a practical means to investigate the impact of cooling temperature and surface wettability on water-harvesting performance. For comparison, we selected four representative data sets from the initial nine, which significantly differed based on surface wettability and the amount of water collected in response to changes in cooling temperature. Fig. 5a–d compare the mass of collected water per unit area for four glass substrates (superhydrophilic, hydrophilic, hydrophobic, and superhydrophobic) as the collection time increases. As shown in Fig. S5,† the collection mass of all substrates showed an inflection time point between 10 and 30 min at which condensed water droplets begin to fall. Afterwards, the mass linearly varies with the slope at all cooling temperatures and monotonically increases with time, showing that the water is collected at a constant rate. The  $R^2$  value of all linear fitting lines is 0.98 or higher, indicating that the water harvesting weight maintains a best-fit linear regression line over time. The water collection rate, which is obtained by dividing

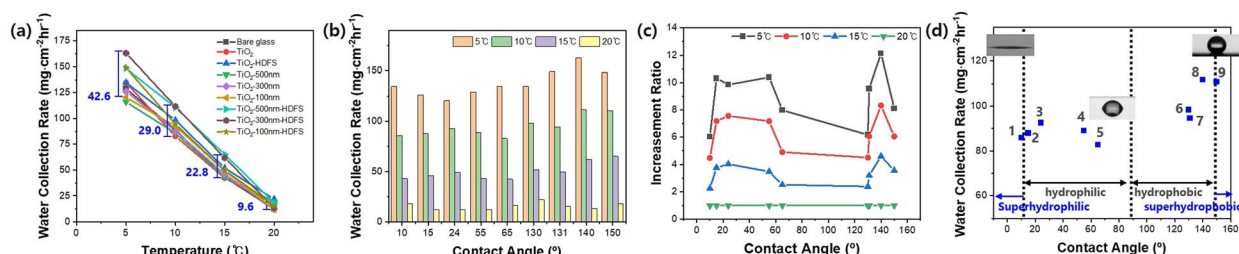


Fig. 6 Water collection rate of various surface structures obtained for 5 h as a function of (a) the incline of cooling temperature and (b) the contact angle of various glasses. (c) Normalized enhancement ratio of water collection rate with cooling temperature based on harvesting rate of each glass at  $20^\circ\text{C}$ . (d) The relationship between contact angle and surface wettability of nine samples and water collection rate of each glass at  $10^\circ\text{C}$  with contact angle and surface wettability. (1:  $\text{TiO}_2$  500 nm, 2:  $\text{TiO}_2$  300 nm, 3:  $\text{TiO}_2$  100 nm, 4: plain glass, 5: 1: bare  $\text{TiO}_2$ , 6: bare  $\text{TiO}_2$  HDFs, 7:  $\text{TiO}_2$  100 nm HDFs, 8:  $\text{TiO}_2$  300 nm HDFs, 9:  $\text{TiO}_2$  500 nm HDFs).

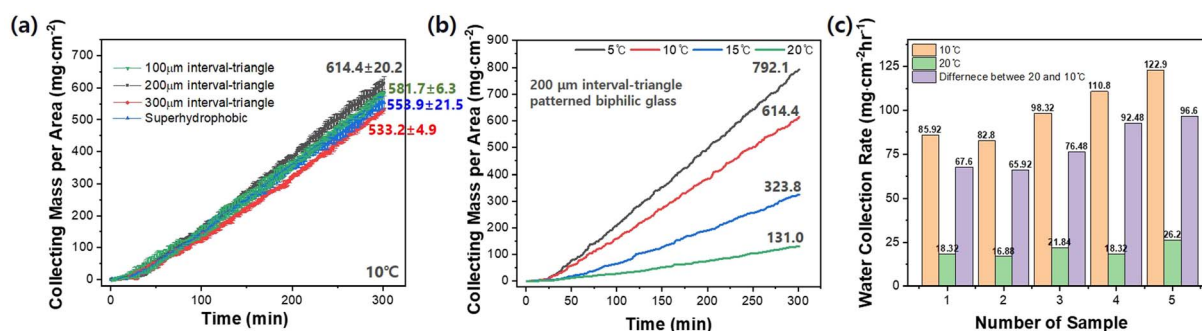


Fig. 7 (a) Water-collecting mass per unit area of biphilic and superhydrophobic glasses obtained for 5 h as a function of the collecting time at 10 °C and the average value of four measurement points with standard deviation (b) water collecting amounts of biphilic glass (200 μm interval-60 μm height triangle) as a function of collecting time for 5 h with the cooling temperature. (c) Comparison of water collection rate and the difference between water collection rate of each glass harvested for 5 h at 20 and 10 °C of cooling temperature: (1) superhydrophilic, (2) hydrophilic, (3) hydrophobic, (4) superhydrophobic, and (5) best biphilic (200 μm interval-60 μm height triangle).

the cumulative weight by the product of unit area and time, increases gradually until the amount of condensation and removal reaches equilibrium, and then saturates. It starts at a low level and then saturates after a certain period. In the beginning, condensation and growth occur, but over time the amount of removed water droplets increases, and the water collection rate saturates. As the cooling temperature decreases, the amount of condensed water droplets and the water collection rate significantly increase, resulting in a slightly longer time needed to achieve saturation for water droplet removal.

Fig. 6a shows the water collection rate of nine glass substrates with varying surfaces as a function of the cooling temperature. The condensation rate increases as the cooling temperature decreases, collecting more water. The impact of surface properties on the water harvesting efficiency is more pronounced at lower temperatures, leading to more significant variations in the efficiency. We found that lowering the cooling temperature is more efficient than fabricating complex surface structures on the window glass, as there is a limit to the maximum water harvesting efficiency that can be achieved using the three-dimensional bio-mimetic structure. Fig. 6b compares the AWH efficiency obtained at an underground cooling-capable temperature of 10 °C and a typical ambient temperature of 20 °C and the difference in the water collection rate between the two temperatures. The underground cooling method can reach a temperature of around 10 °C. The water harvesting rate of the plain glass substrate increases 7.2-fold from 12.4 to 89.0 mg cm<sup>-2</sup> h<sup>-1</sup> when the cooling temperature is decreased from 20 °C to 10 °C. Glass substrate with a surface of 300 nm high TiO<sub>2</sub> nanopillars, and a contact angle of 140° was the most efficient, achieving a water harvesting rate of 111.8 mg cm<sup>-2</sup> h<sup>-1</sup> at 10 °C. However, this represents only a 25.6% improvement over plain glass substrates at the same temperature. Fig. 6c displays the normalized enhancement ratio for all glass substrates, calculated based on the harvesting rate at 20 °C. The figure demonstrates that the ratio of the harvesting rate increases more significantly in the hydrophobic region, where the contact angle is between 130 and 150°, and the hydrophilic region, where the contact angle is between 10 and 55° as the

cooling temperature decreases. Fig. 6d demonstrates that the highest water harvesting rate at 10 °C occurs in a narrow boundary region between hydrophobic and superhydrophobic surfaces, whereas other surfaces exhibit similarly low performance. Although the introduction of 2D nanopillar structures provides some improvement over other flat surfaces, it requires a much more significant increase in rate than the increment of water collection rate shown in the present experiment to justify the effort needed to create such structures. It is noteworthy that lowering the cooling temperature can still yield a considerable amount of water collection.

Fig. 7a compares the water harvesting mass per unit area of three different hydrophilic micropattern-hydrophobic backgrounds, referred to as biphilic surfaces, at 10 °C as a function of time. The glass substrate with a biphilic surface period of a 200 μm triangle pattern exhibits the highest water harvesting rate. However, it only outperforms other biphilic and superhydrophobic glass substrates slightly. In general, most biphilic substrates show good water harvesting efficiency. As presented in Fig. 7b, the relationship between water harvesting performance and cooling temperature for biphilic glass substrates is similar to that of other single surface wettability substrates described earlier. Fig. 7c compares the water harvesting capacities of five glass substrates with different surface wettabilities at 10 °C and 20 °C, focusing on the water harvesting performance near 10 °C for potential use in underground cooling systems. As shown, the biphilic surface has the highest water harvesting rate at both temperatures.<sup>40–43</sup> However, it is reconfirmed that introducing the micro-patterned 2D nanopillar structure to the glass substrate alone does not significantly improve the water harvesting efficiency. While surface structural change did not significantly increase the water harvesting efficiency, cooling the surface temperature significantly impacted the efficiency for all different substrates tested in the study.

For instance, although the hydrophilic glass substrate without structural change showed the lowest water harvesting efficiency at the same cooling temperature, its efficiency increased to a meaningful value when cooled to 10 °C. Thus, to





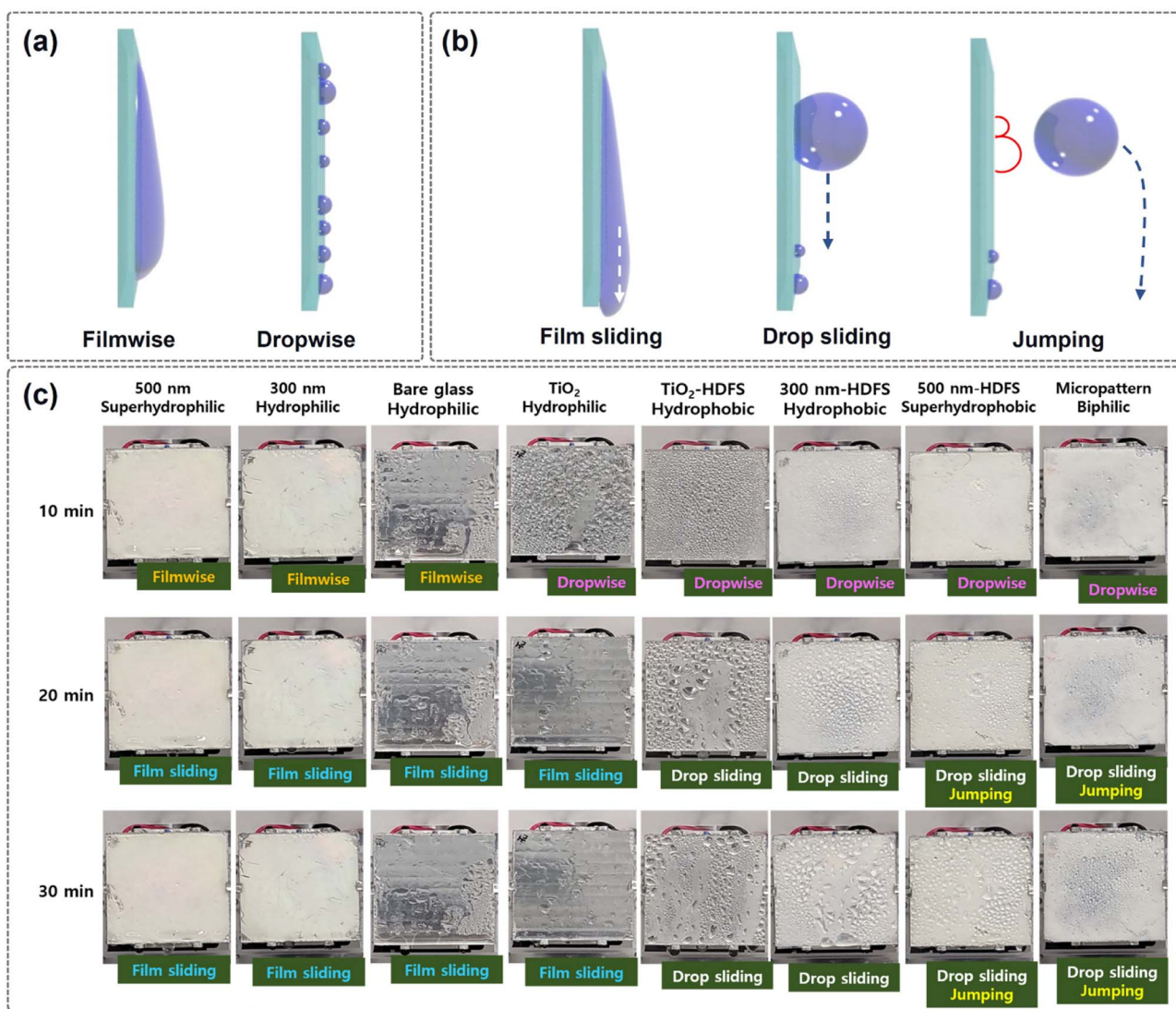


Fig. 8 Schematic of (a) the water condensation: filmwise and dropwise and (b) the water removal: film sliding, drop sliding, and jumping. (c) Photo images showing shedding phenomena on various surfaces with exposure time to mist at 10 °C of cooling temperature.

achieve effective water harvesting, temperature control is imperative. Fig. 8 displays schematic and actual images of the water condensation and sliding behavior on different surfaces. To compare the water collection behavior, images were

captured using a smartphone camera. Hydrophilic surfaces, such as 2D nanopillar-coated and plain glass surfaces, have low contact angles (<55°) and exhibit filmwise condensation. The water films grow and merge with adjacent films until they

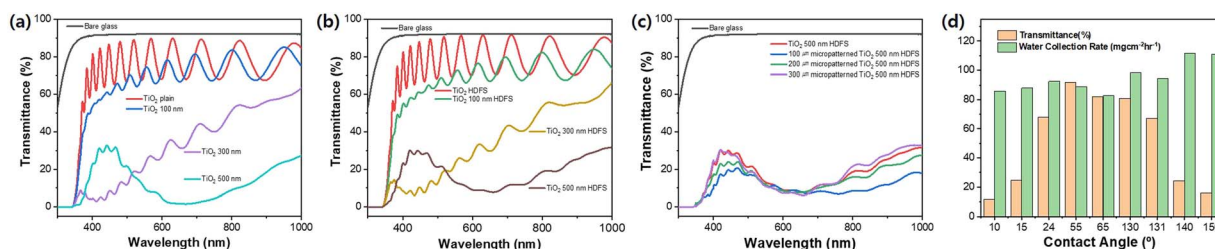


Fig. 9 Transmittance spectra of various surface structures of the glass with the wettability of surface structure: (a) TiO<sub>2</sub> 2D nanopillar arrays (100, 300, 500 nm), (b) HDFS-coated 2D TiO<sub>2</sub> plain and TiO<sub>2</sub> nanopillar arrays (100, 300, 500 nm), (c) HDFS-removed micropattern-HDFS-coated nanopillar background. (d) Transmittance variation of various surface structures of the glass with the contact angle of surface structure.

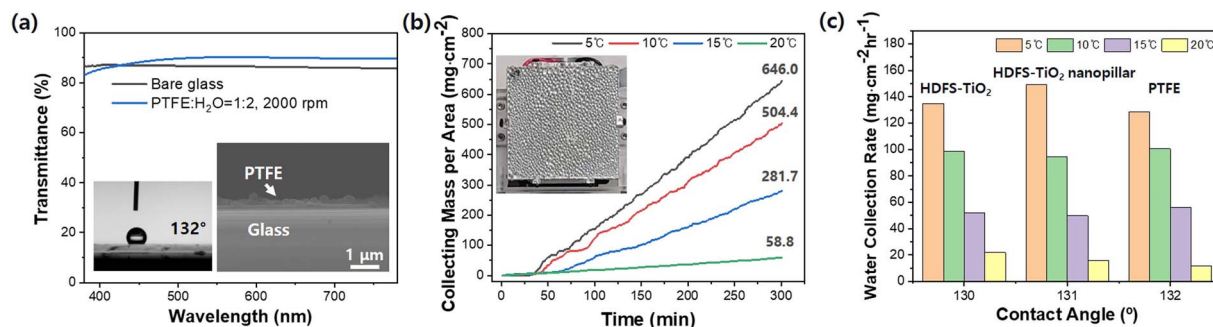


Fig. 10 (a) Transmittance spectrum of PTFE coated glass substrate (left-handed inset: contact angle, right-handed inset: SEM picture) (b) water collecting mass per unit area and (c) water collection rate of three different hydrophobic glass substrates with collecting temperature; (1) HDFs–TiO<sub>2</sub> coated glass, (2) HDFs–TiO<sub>2</sub> 100 nm nanopillar coated glass, (3) PTFE coated glass substrate.

become heavy enough to slide down and condense again. On the other hand, hydrophobic HDFs-coated glass surfaces have high contact angles ( $>130^\circ$ ) and display dropwise condensation. The condensed droplets grow and merge until they become large enough to slide down and condense again. TiO<sub>2</sub>-coated glass is an exception, exhibiting a combination of droplet and filmwise condensation. Superhydrophobic or biphilic glass substrates form tiny droplets initially, but they quickly jump and fall off the surface. This jumping behavior could be attributed to the elastic motion of a fused droplet as it quickly recovers its globular shape upon fusion. As time passes, more droplets form and jump together with sliding. The highest water harvesting efficiency of the biphilic surface is achieved through the cooperation of fast water capturing and condensation speed on the hydrophilic area and enhanced water sliding speed on the hydrophobic region. This indicates that surface wetting varies depending on the surface structure. It also shows that the condensation, growth, and removal mechanism of water droplets change considerably with substrate wettability.

The difference in cooling temperature has a more significant impact on the water harvesting efficiency than the difference in water growth and removal caused by surface wettability. When the cooling temperature drops below 10 °C, the speed of condensation by capturing water from the air dominates over the increased growth and removal speed of droplets by the surface structure. The optical transmittance of window glass is critical to ensure a clear view.

Fig. 9 compares the transmittance spectra of glass substrates with different surface wettability used in the experiment. Plain glass has a transmittance of 92% of the full range of visible light, while glass coated with 800 nm of TiO<sub>2</sub> thin film has a transmittance of 81% to 82% regardless of whether a HDFs coating is applied, but an optical interference pattern is present. 2D nanopillars, which were introduced to control surface wettability, reduce the transmittance as the height increases, causing the appearance of fog. A hydrophobic or biphilic surface with a contact angle of 130–150° and high-water harvesting rate reduces the transmittance to below 25%. This means that using 2D nanopillars in hydrophilic or hydrophobic window glass is inappropriate as the manufacturing process is

complicated and costly, and low transmittance deteriorates the visibility (Fig. S6†).

Our results indicate that a simple, cost-effective, and optically transparent coating approach is required to manufacture AWH window glass with contact angles of 130–140° and transmittance over 80% for the atmospheric water harvesting process at low temperatures. Therefore, we selected a simple spin-coating process using a polytetrafluoroethylene (PTFE) nanoparticle solution to fabricate a hydrophobic nanofilm on the glass surface with a contact angle higher than 130°. By adjusting the concentration and spin speed of the PTFE polymer nanoparticle solution, we precisely controlled the thickness, contact angle, and transmittance of the PTFE nanofilms, as shown in Fig. S7 and S8.† We determined the appropriate concentration and spin speed by optimizing the process for maximum transmittance and contact angle. Fig. 10a shows a cross-sectional SEM photograph of the optimal PTFE nanofilm, contact angle, and transmittance. The appropriate PTFE thin film was obtained by spin-coating a solution having a 1 : 2 volume ratio with water at 2000 rpm for 60 seconds, resulting in a thickness of 200–300 nm and a contact angle of 131°. Due to the decreased anti-reflection (AR) effect, the transmittance reached 95%, which is higher than that of the plain glass substrate. Fig. 10b shows the increase in water harvesting weight with increasing water collection time and decreasing cooling temperature. It demonstrates that the water harvesting rate increases from 11.7 to 100.5 mg cm<sup>-2</sup> h<sup>-1</sup> when the cooling temperature is decreased from 20 to 10 °C. The water harvesting rate was calculated using the time-change graph of the water harvesting weight. We compared the water harvesting rate of the PTFE nanofilm-coated glass and HDFs-coated plain TiO<sub>2</sub> and 2D TiO<sub>2</sub> nanopillar-coated glass with 130 and 131° contact angles.

Fig. S9† exhibits a water collection mechanism that combines dropwise condensation and drop-sliding removal processes. The water drops are more uniformly distributed on the PTFE nanofilm-coated glass than on the nanopatterned glass because of the more uniformly-coated film of PTFE on the glass. The results show that the water harvesting efficiency of the PTFE nanofilm-coated glass is comparable to that of the HDFs-coated plain TiO<sub>2</sub> and 2D TiO<sub>2</sub> nanopillar glass substrates. Regardless of whether one layer PTFE, two layer





HDFS/TiO<sub>2</sub>, or two layer HDFS/TiO<sub>2</sub> based nanopillars are employed, if the contact angle is similar in a hydrophobic range (130–132°), the water harvesting efficiency is similar. If an underground cooling system can cool down the window glass, using a glass substrate coated with a PTFE nano-thin film with a contact angle of 132° on the window surface would be suitable, compared to the more complex structure of hydrophobic TiO<sub>2</sub>-coated glasses.

## 4. Conclusion

We investigated the effects of cooling temperature and surface wettability of glass substrates on water harvesting efficiency through fog mist condensation. We quantified mist condensation and subsequent dropping rates on vertical glass surfaces with a wide range of wettability as measures of water harvesting efficiency. Consistent with previous reports on fog-basking, we found that glass surfaces with hydrophilic patterns on hydrophobic backgrounds, *i.e.*, biphilic surfaces, had the highest AWH efficiency during the formation of water droplets in dynamic mist flows, compared to uniform hydrophilic or hydrophobic surfaces. However, we also observed that the effect of cooling temperature on atmospheric water harvesting (AWH) efficiency on the glass surface was more significant than the effect of surface wettability. This observation is consistent with the efficient water collection under static air by Australian frogs and lizards, which reduce their skin temperature by cold blood to harvest moisture despite having uniform hydrophilic skin surfaces. It can be assumed that beetles in the Namib desert have the most efficient biphilic surface in water harvesting because they cannot lower the skin surface temperature except for when they are exposed to the low temperature of the desert dawn. Lowering the temperature has a much more significant effect on increasing the condensation rate than improving the condensation, growth, and removal rate through surface wettability characteristics, and thus significantly improves water collection efficiency. The cooling temperature that can be achieved with the underground cooling system is a minimum of 10–15 °C. At 10 °C, the AWH rate of plain glass is 89.0 mg cm<sup>-2</sup> h<sup>-1</sup>, which is 7.2 times higher than the AWH rate of 12.4 mg cm<sup>-2</sup> h<sup>-1</sup> at 20 °C. On the other hand, at 10 °C, changing the plain glass to a biphilic surface improves the AWH rate by only 1.26 times to 111.84 mg cm<sup>-2</sup> h<sup>-1</sup>. Therefore, lowering the temperature is a more practical approach to achieve high AWH efficiency than the complex processes and efforts required to create the most efficient biphilic structure on the window glass surface if sustainable cooling energy can be supplied. Our results will be helpful in future water harvesting applications for window glasses connected to underground cooling systems.

## Author contributions

Yoonseo Do: conceptualization, investigation, data curation, writing – original draft. Minji Ko: methodology, visualization, data curation. Young Kwang Lee: conceptualization, project administration, writing – review & editing. All authors read and approved the final manuscript.

## Conflicts of interest

There are no conflicts to declare.

## Acknowledgements

This work was supported by a volunteer lab researcher program of San Diego State University.

## References

- 1 M. M. Mekonnen and A. Y. Hoekstra, *Sci. Adv.*, 2016, **2**, e1500323.
- 2 A. A. Salehi, M. Ghannadi-Maragheh, M. Torab-Mostaedi, R. Torkaman and M. Asadollahzadeh, *Renewable Sustainable Energy Rev.*, 2020, **120**, 109627.
- 3 X. Wang, J. Zeng, J. Li, X. Yu, Z. Wang and Y. Zhang, *J. Mater. Chem. A*, 2021, **9**, 1507–1516.
- 4 A. LaPotin, H. Kim, S. R. Rao and E. N. Wang, *Acc. Chem. Res.*, 2019, **52**, 1588–1597.
- 5 V. G. Gude, *Rev. Environ. Sci. Bio/Technol.*, 2017, **16**, 591–609.
- 6 X. Zhou, H. Lu, F. Zhao and G. Yu, *ACS Mater. Lett.*, 2020, **2**, 671–684.
- 7 M. Elimelech and W. A. Phillip, *Science*, 2011, **333**, 712–717.
- 8 X. Zhou, F. Zhao, P. Zhang and G. Yu, *ACS Mater. Lett.*, 2021, **3**, 1112–1129.
- 9 H. Jarimi, R. Powell and S. Riffat, *Int. J. Low-Carbon Technol.*, 2020, **15**, 253–276.
- 10 M. Tomaszewicz, M. A. Najm, D. Beysens, I. Alameddine and M. El-Fadel, *Environ. Rev.*, 2015, **23**, 425–442.
- 11 K. Yang, T. Pan, Q. Lei, X. Dong, Q. Cheng and Y. Han, *Environ. Sci. Technol.*, 2021, **55**, 6542–6560.
- 12 B. Wang, X. Zhou, Z. Guo and W. Liu, *Nano Today*, 2021, **40**, 101283.
- 13 K. C. Park, P. Kim, A. Grinthal, N. He, D. Fox, J. C. Weaver and J. Aizenberg, *Nature*, 2016, **531**, 78–82.
- 14 L. Liu, S. Wang, X. Zeng, P. Pi and X. Wen, *Adv. Mater. Interfaces*, 2021, **8**, 2101603.
- 15 M. Edalatpour, L. Liu, A. M. Jacobi, K. F. Eid and A. D. Sommers, *Appl. Energy*, 2018, **222**, 967–992.
- 16 C. R. Tracy, N. Laurence and K. A. Christian, *Am. Nat.*, 2011, **178**, 553–558.
- 17 P. Comanns, C. Effertz, F. Hischen, K. Staudt, W. Böhme and W. Baumgartner, *Beilstein J. Nanotechnol.*, 2011, **2**, 204–214.
- 18 I. Scholz, W. J. P. Barnes, J. M. Smith and W. Baumgartner, *J. Exp. Biol.*, 2009, **212**, 155–162.
- 19 P. Comanns, *J. Exp. Biol.*, 2018, **221**, jeb153130.
- 20 X. Liu, J. Trosseille, A. Mongruel, F. Marty, P. Basset, J. Laurent, L. Royon, T. Cui, D. Beysens and T. Bourouina, *iScience*, 2021, **24**, 102714.
- 21 S.-H. Wu and M. L. Povinelli, *Opt. Express*, 2015, **23**, A1363–A1372.
- 22 W. Li, Y. Shi, K. Chen, L. Zhu and S. Fan, *ACS Photonics*, 2017, **4**, 774–782.
- 23 W. E. Alnaser and A. Barakat, *Appl. Energy*, 2000, **65**, 3–18.
- 24 L. Zhu, A. Raman, K. X. Wang, M. A. Anoma and S. Fan, *Optica*, 2014, **1**, 32–38.



- 25 J. F. Maestre-Valero, V. Martínez-Alvarez and A. Baille, *J. Hydrol.*, 2012, **460–461**, 103–109.
- 26 G. Sharan, D. Beysens and I. Milimouk-Melnytschouk, *J. Arid Environ.*, 2007, **69**, 259–269.
- 27 G. Sharan, *Int. J. Res. Serv. Learn. Eng.*, 2011, **6**, 130–150.
- 28 Y. Zhai, Y. G. Ma, S. N. David, D. L. Zhao, R. Lou, G. Tan, R. Yang and X. Yin, *Science*, 2017, **355**, 1062–1066.
- 29 C. Dorrer and J. Rühe, *Adv. Mater.*, 2008, **20**, 159–163.
- 30 J. Xu, J. Zhang, B. Fu, C. Song, W. Shang, P. Tao and T. Deng, *ACS Appl. Mater. Interfaces*, 2020, **12**, 47612–47622.
- 31 X. Liu, D. Beysens and T. Bourouina, *ACS Mater. Lett.*, 2022, **4**, 1003–1024.
- 32 J. Lindblom and B. Nordell, *Desalination*, 2006, **189**, 248–260.
- 33 *Smart Houses Portugal*, from, <https://www.ecopassivehouses.com/canadian-wells/>.
- 34 *Simple Geothermal Air Cooling*, from, <https://www.reuk.co.uk/wordpress/geothermal/simple-geothermal-air-heating-and-cooling/>.
- 35 J. M. A. Márquez, M. Á. M. Bohórquez and S. G. Melgar, *Sensors*, 2016, **16**, 306.
- 36 A. Balachandran, H. Parayilkalapurackal, S. Rajpoot and S. Lone, *ACS Appl. Bio Mater.*, 2023, **6**, 44–63.
- 37 B. Bhushan, *Philos. Trans. R. Soc., A*, 2019, **377**, 20190119.
- 38 H. Zhu, Z. Guo and W. Liu, *Chem. Commun.*, 2016, **52**, 3863–3879.
- 39 S. J. Lee, N. Ha and H. Kim, *ACS Sustainable Chem. Eng.*, 2019, **7**, 10561–10569.
- 40 T. Xu, Y. Lin, M. Zhang, W. Shi and Y. Zheng, *ACS Nano*, 2016, **10**, 10681–10688.
- 41 C. Wen, H. Guo, H. Bai, T. Xu, M. Liu, J. Yang, Y. Zhu, W. Zhao, J. Zjang, M. Cao and L. Zhang, *ACS Appl. Mater. Interfaces*, 2019, **11**, 34330–34337.
- 42 J. Ju, K. Xiao, X. Yao, H. Bai and L. Jiang, *Adv. Mater.*, 2013, **25**, 5937–5942.
- 43 H. Bai, C. Zhang, Z. Logn, H. Geng, T. Ba, Y. Fan, C. Yu, K. Li, M. Cao and L. Jiang, *J. Mater. Chem. A*, 2018, **6**, 20966–20972.
- 44 A. Marmur, *Langmuir*, 2004, **20**, 3517–3519.
- 45 S. S. Latthe, C. Terashima, K. Nakata and A. Fujishima, *Molecules*, 2014, **19**, 4256–4283.
- 46 S. F. Ahmed, M. M. K. Khan, M. T. O. Amanullah, M. G. Rasul and N. M. S. Hassan, *Renewable Energy*, 2021, **172**, 350–367.
- 47 R. Vidhi, *Energies*, 2018, **11**, 2941.
- 48 Y. Jin, L. Zhang and P. Wang, *Global Chall.*, 2017, **1**, 1700019.
- 49 K. Hou, X. Li, Q. Li and X. Chen, *Adv. Mater. Interfaces*, 2020, **7**, 1901683.
- 50 K. Gerasopoulos, W. L. Luedeman, E. Ölçeroglu, M. McCarthy and J. J. Benkoski, *ACS Appl. Mater. Interfaces*, 2018, **10**, 4066–4076.
- 51 J. Trosseille, A. Mongruel, L. Royon, M. G. Medici and D. Beysens, *Eur. Phys. J. E: Soft Matter Biol. Phys.*, 2018, **42**, 144.
- 52 Y. Zhai, Y. Ma, S. N. David, D. Zhao, R. Lou, G. Tan, R. Yang and X. Yin, *Science*, 2017, **355**, 1062–1066.
- 53 M. S. Ahsan, F. Dewanda, M. S. Lee, H. Sekita and T. Sumiyoshi, *Appl. Surf. Sci.*, 2013, **265**, 784–789.
- 54 H. Bai, L. Wang, J. Ju, R. Sun, Y. Zheng and L. Jiang, *Adv. Mater.*, 2014, **26**, 5025–5030.
- 55 E. Kostal, S. Stroj, S. Kasemann, V. Matylitsky and M. Domke, *Langmuir*, 2018, **34**, 2933–2941.
- 56 N. Bakhtiari, S. Azizian and B. Jaleh, *J. Colloid Interface Sci.*, 2022, **625**, 383–396.
- 57 J. Lu, C.-V. Ngo, S. C. Singh, J. Yang, W. Xin, Z. Yu and C. Guo, *Langmuir*, 2019, **35**, 3562–3567.
- 58 Y. K. Lee, J. R. Oh and Y. R. Do, *Appl. Phys. Lett.*, 2007, **91**, 041907.
- 59 X. Wang, J. Zeng, X. Yu, C. Liang and Y. Zhang, *Appl. Surf. Sci.*, 2019, **465**, 986–994.
- 60 T. Kamegawa, Y. Shimizu and H. Yamashita, *Adv. Mater.*, 2012, **24**, 3697–3700.
- 61 Y. Lai, J. Huang, Z. Cui, M. Ge, K.-Q. Zahng, Z. Chen and L. Chi, *Small*, 2016, **12**, 2203–2224.

